

1 **Enhanced pore space analysis by use of μ -CT, MIP,**
2 **NMR, and SIP**

3

4 Zeyu Zhang ¹, Sabine Kruschwitz ^{2,3}, Andreas Weller ⁴, Matthias Halisch ⁵

5

6 ¹ Southwest Petroleum University, School of Geoscience and Technology, 610500 Chengdu, China

7 ² Federal Institute for Material Research and Testing (BAM), D-12205 Berlin, Germany

8 ³ Technische Universität Berlin, Institute of Civil Engineering, D-13355 Berlin, Germany

9 ⁴ Clausthal University of Technology, Institute of Geophysics, D-38678 Clausthal-Zellerfeld, Germany

10 ⁵ Leibniz Institute for Applied Geophysics (LIAG), D-30655 Hannover, Germany

11 *Correspondence to: Zeyu Zhang (zeyuzhangchina@163.com)*

12

13

14

15

16

17

18

19

20

21

22

23

24

25

26

27

28

29

30

31

32

33 **Abstract**

34 We investigate the pore space of rock samples with respect to different petrophysical parameters using
35 various methods, which provide data upon pore size distributions, including micro computed tomography
36 (μ -CT), mercury intrusion porosimetry (MIP), nuclear magnetic resonance (NMR), and spectral induced
37 polarization (SIP). The resulting cumulative distributions of pore volume as a function of pore size are
38 compared. Considering that the methods differ with regard to their limits of resolution, a multiple length
39 scale characterization of the pore space is proposed, that is based on a combination of the results from all of
40 these methods. The approach is demonstrated using samples of Bentheimer and Röttbacher sandstone.
41 Additionally, we compare the potential of SIP to provide a pore size distribution with other commonly used
42 methods (MIP, NMR). The limits of resolution of SIP depend on the usable frequency range (between
43 0.002 Hz and 100 Hz). The methods with similar resolution show a similar behavior of the cumulative pore
44 volume distribution in the overlapping pore size range. We assume that μ -CT and NMR provide the pore
45 body size while MIP and SIP characterize the pore throat size. Our study shows that a good agreement
46 between the pore radii distributions can only be achieved if the curves are adjusted considering the
47 resolution and pore volume in the relevant range of pore radii. The MIP curve with the widest range in
48 resolution should be used as reference.

49

50 Keywords: Pore Space Analysis, Joint Methods, Fractal Dimension, Spectral Induced Polarization

51 **1 Introduction**

52 Transport and storage properties of reservoir rocks are determined by the size and arrangement of the pores.
53 In this paper we use the term geometry to refer to the relevant pore sizes, such as the pore throat radius,
54 pore body radius, body to throat ratio, shape of the pore, and pore volume corresponding to certain pore
55 radius. Different methods have been developed to determine the pore size distribution of rocks. These
56 methods are based on different physical principles. Therefore, it can be expected that the methods
57 recognize different geometries and sizes. Additionally, the ranges of pore sizes that are resolved by the
58 methods are different (Meyer et al., 1997). Rouquerol et al. (1994) stated in the conclusions of their
59 recommendations for the characterization of porous solids that no experimental method provides the
60 absolute value of parameters such as porosity, pore size, surface area, and surface roughness. It should be
61 noted that these parameters indicate a fractal nature. That means that the value of the parameter depends on
62 the spatial resolution of the method.

63 An enhanced pore space analysis using different methods should be able to provide a better description of
64 the pore space over a wide range of pore sizes. Our study of pore space analysis is based on the following
65 methods: micro computed tomography (μ -CT), mercury intrusion porosimetry (MIP), nuclear magnetic

66 resonance (NMR), and spectral induced polarization (SIP). The first three methods can be regarded as
67 standard methods to derive a pore size distribution. Since these methods can reveal the inner structure of
68 the rocks, they are widely applied in geosciences (e.g. Halisch et al., 2016b, Mees et al., 2003,
69 Behroozmand et al., 2015, Weller et al., 2015). The main aim of our paper is to integrate an electrical
70 method in this study. Electrical conductivity and polarizability (or real and imaginary part of electrical
71 conductivity) are fundamental physical properties of porous materials. The SIP method measures the low-
72 frequency electric behavior of rocks and soil material that can be efficiently represented by a complex
73 electric conductivity (e.g. Slater and Lesmes, 2002). The electric properties of a porous material depend to
74 a large extent on key parameters including the porosity, the grain and pore size distribution, the specific
75 internal surface, the tortuosity, the saturation and the chemical composition of the pore-filling fluids. SIP is
76 a non-destructive method that can be applied to characterize the geometry of the pore system. The use of
77 SIP in this field has been reported only recently (Revil et al., 2014; Niu and Zhang, 2017, Zhang et al.,
78 2017).

79 We are aware that further methods can be applied for the characterization of pore size distribution, e.g.
80 synchrotron-radiation-based computed tomography (Peth et al., 2008), focused ion beam tomography
81 (Keller et al., 2011), transmission electron microscopy (Gaboreau et al., 2012), scanning electron
82 microscopy (SEM), ¹⁴C labeled methylmethacrylate method (Kelokaski et al., 2005), and gas adsorption
83 and desorption method (BET) (Avnir and Jaroniec, 1989).

84 Our study presents an approach to describe and quantify the pore space of porous material by combining
85 the results of methods with different resolution. Samples of Bentheimer and Röttbacher sandstone are
86 investigated by μ -CT, MIP, NMR, and SIP. Each method provides the pore size distribution in a limited
87 range of resolution. It is not our intention to combine the data of the different methods in a joint inversion
88 to get a more reliable pore size distribution as proposed by Niu and Zhang (2017). We prefer to compare
89 the resulting pore size distributions to each other to get two different pore radii distributions, one for the
90 pore body radius and one for the pore throat radius. The comparison of the two curves enables the
91 determination of the ratio between pore body and pore throat radius. A joint inversion that ignores the
92 difference between pore body and pore throat provides a simplified model that ignores the complexity of
93 pore space geometry.

94 Considering the fractal nature of pore space geometry an attempt is made to determine the fractal
95 dimension of the pore volume distribution for the two investigated samples. The fractal dimension is a
96 useful parameter for up-and downscaling of geometrical quantities. Zhang and Weller (2014) investigated
97 the fractal behavior of the pore volume distribution by capillary pressure curves and NMR T_2 distributions
98 of sandstones. Considering the differences in fractal dimension resulting from the two methods, they
99 concluded a differentiation into surface dimension and volume dimension. Additionally, the fractal
100 dimension is used in methods of permeability prediction (e.g. Pape et al., 2009).

101 2 Theory

102 The pore size distribution resulting from different methods has to be compared and evaluated. We prefer a
103 comparison based on the cumulative volume fraction of pores V_c , which is expressed by

$$104 \quad V_c = \frac{V(< r)}{V_p}, \quad (1)$$

105 with V_p being the total pore volume, and $V(< r)$ the cumulative volume of pores with radii less than r . A
106 graph displaying the logarithm of V_c versus the logarithm of the pore radius offers the advantage that the
107 slope of the curves is related to the fractal dimension of the pore volume (Zhang and Weller, 2014).

108 Fractal theory is applied to describe the structure of geometric objects (Mandelbrot, 1977, 1983). At
109 molecular size and microscopic range, surfaces of most materials including those of natural rocks show
110 irregularities and defects that appear to be self-similar upon variation of resolution (Avnir et. al, 1984). A
111 self-similar object is characterized by similar structures at different scales. The regularity of self-similar
112 structures can be quantified by the parameter of fractal dimension D . Pape et al. (1982) first proposed a
113 fractal model (the so called ‘pigeon-hole model’ or ‘Clausthal Concept’) for the geometry of rock pores.
114 Fractal dimension describes the size of geometric objects as a function of resolution. This parameter has
115 proved to be useful in the comparison of different methods that determine distributions of pores in
116 sandstones and carbonates (e.g. Zhang and Weller, 2014, Ding et al., 2017).

117 From MIP, the entry sizes of pores and cavities, which is referred to as pore throat radius r_t , can be
118 determined according to the Washburn-equation (Washburn, 1921)

$$119 \quad r_t = -\frac{2 \cdot \gamma \cdot \cos \theta}{P_c}, \quad (2)$$

120 with $\gamma = 0.48$ N/m being the surface tension of mercury, $\theta = 140^\circ$ the contact angle between mercury and
121 the solid minerals, and P_c the pressure of the liquid mercury that is referred to as capillary pressure.

122 Starting with low pressure, the pores with larger pore throats are filled with mercury. While increasing the
123 pressure, the pores with smaller throats are filled. Reaching a certain pressure level P_c , a cumulative
124 volume of mercury (V_{Hg}) has intruded into the sample that corresponds to the pore volume being accessible
125 by pore throat radii larger or equal r_t according to Eq. (2). Figure 1 shows a 2D image of the pore space of
126 sample BH5-2 (information is given in Section 3) indicating the pore throat radius r_t as measured by MIP
127 by red arrows. Fluid flow properties, and hence the injection pressure of mercury, solely depends upon the
128 narrowest pore diameter in the flow path that corresponds to the pore throat diameter. The cumulative
129 volume of mercury V_{Hg} corresponds to the pore volume $V(>r_t)$. It should be noted that the volume of larger
130 pores, which are shielded by narrower throats, is attributed to the pore throat radius (e.g. Kruschwitz et al.,
131 2016). Knowing the total pore volume V_p , the saturation of the sample with mercury S_{Hg} can be determined.
132 A conventional capillary pressure curve displays the relationship between the saturation of the sample with

133 mercury S_{Hg} as a function of capillary pressure P_c (e.g. Thomeer, 1960). Using the following simple
134 transformations

$$135 \quad S_{Hg} = \frac{V_{Hg}}{V_p} = \frac{V(> r_t)}{V_p} = \frac{V_p - V(< r_t)}{V_p} = 1 - V_c, \quad (3)$$

136 the cumulative volume fraction of pores V_c as defined in Eq. (1) can be determined as a function of r_t .
137 The NMR relaxometry experiment records the decay of transversal magnetization. The measured
138 transversal decay curve is decomposed in a distribution of relaxation times $b(T_2)$. The individual relaxation
139 time T_2 is attributed to a pore space with a certain surface to volume ratio A/V by

$$140 \quad \frac{1}{T_2} = \rho \left(\frac{A}{V} \right), \quad (4)$$

141 with ρ being the surface relaxivity. Considering that for a capillary tube model with cylindrical pores of
142 radius r , the surface to volume ratio equals $2/r$, we get the following linear relationship between pore radius
143 r and relaxation time T_2 (e.g. Kleinberg, 1996):

$$144 \quad r = 2\rho T_2. \quad (5)$$

145 It should be noted that the NMR method resolves the radius r_b that corresponds to the maximal distance to
146 the pore wall. It can be represented by the pore radius of the largest sphere that can be placed inside this
147 pore as shown in Figure 1.

148 Another approach to derive a pore size distribution is based on the SIP method (Revil et al., 2014; Zhang et
149 al., 2017). Relations between grain or pore size and IP parameters have been reported in a variety of studies
150 (e.g. Slater and Lesmes, 2002; Scott and Barker, 2003; Binley et al., 2005; Leroy et al., 2008; Revil and
151 Florsch, 2010). Polarization effects of natural material are caused by different charging and discharging
152 processes of some polarizing elements such as grain surface, pore throat, membrane, and electrical double
153 layer. Following an approach proposed by Schwarz (1992), the complex conductivity of an individual
154 polarization element can be presented by a Debye model. It is assumed that the recorded spectra result from
155 a superposition of polarization processes characterized by different relaxation times. This approach has
156 been adopted to generate synthetic spectra of electrical conductivity from distributions of grain sizes (e.g.
157 Revil and Florsch, 2010) or pore sizes (e.g. Niu and Zhang, 2017). A decomposition of the spectra is
158 needed to derive the relaxation time distribution. Florsch et al. (2014) demonstrated that a variety of models
159 can be used as kernel for the decomposition of the spectra. Revil et al. (2014) compare the results of Debye
160 and Warburg decomposition. According to our opinion, there are no clear indications for superiority of the
161 Warburg decomposition. Therefore, we prefer to use the Debye decomposition. The algorithm described by
162 Nordsiek and Weller (2008) provides the electrical relaxation time distribution as well as the total
163 chargeability from complex conductivity spectra.

164 According to the assumption that the electrical relaxation time and pore size are related to each other, the
165 specific chargeability at a certain relaxation time corresponds to the pore volume attributed to a certain pore
166 size, and the total chargeability is attributed to the total pore volume of the sample. The volume fraction V_c
167 corresponds to the ratio of cumulative chargeability to total chargeability. To transform the relaxation time
168 distribution into a pore size distribution, we adopt the approach proposed by Schwarz (1962) and applied
169 by Revil et al. (2012) for the Stern layer polarization model:

$$170 \quad r = \sqrt{2\tau D_{(+)}} , \quad (6)$$

171 with $D_{(+)}$ being the diffusion coefficient of the counter-ions in the Stern layer and τ being the relaxation
172 time. Originally, this equation describes the relation between the radius of spherical particles in an
173 electrolyte solution and the resulting relaxation time. Though it remains arguable whether the radius of
174 spherical grains can be simply replaced by the pore radius (Weller et al., 2016), we generally follow this
175 approach. Additionally, we assume a constant diffusion coefficient $D_{(+)} = 3.8 \times 10^{-12}$ m²/s as proposed by
176 Revil (2013).

177 The signal amplitude at a given relaxation time corresponds to the pore volume related to the pore radius
178 determined by Eq. (6). Considering the experience that the polarization is related to the specific surface
179 area per unit pore volume (e.g. Weller et al., 2010), we assume that the IP signals are caused by the ion-
180 selected active zones in the narrow pores that are comparable with the pore throats. Their size is quantified
181 by the pore throat radius r_t . Following the procedure proposed by Zhang et al. (2017), the cumulative
182 volume fraction V_c corresponds to the ratio of cumulative chargeability to total chargeability. Considering
183 the restricted range of pore radii (0.1-25 μ m) resolved by SIP, a correction of the maximum V_c becomes
184 necessary.

185 **3 Samples and methods**

186 For this study, two different sandstone samples have been used: first, a Bentheimer sandstone, sample
187 BH5-2. The shallow-marine Bentheimer sandstone was deposited during the Early Cretaceous (roughly 140
188 million years ago) and forms an important reservoir rock for petroleum (Dubelaar et al., 2015). This
189 sandstone is widely used for systematic core analysis due its simple mineralogy and the quite homogeneous
190 and well-connected pore space. It is composed out of 92% quartz, contains some feldspar and about 2.5
191 vol.-% of kaolinite (Peksa et al., 2015), which is a direct alteration product of the potassium-bearing
192 feldspar minerals. Accordingly, surface area as well as surface relaxivity values are mostly controlled by
193 the kaolinite for this rock.

194 Secondly, a Röttbacher sandstone, sample RÖ10B, has been used. The Röttbacher sandstone is a fine-
195 grained, more muscovite-illite containing, and rather homogeneous material that was deposited during the
196 Lower Triassic era (roughly 250 million years ago). It is suitable for solid stonework and has been widely

197 used as building material for facades as well as for indoor and outdoor flooring. The Röttbacher sandstone
198 was included in a study on the relationship of pore throat sizes and SIP relaxation times reported by
199 Kruschwitz et al. (2016). This sandstone consists mostly of quartz, but features a higher amount of clay
200 minerals than the Bentheimer sample. Additionally, Fe-bearing minerals (e.g. haematite) have been formed
201 during its arid depositional environment, giving this sandstone a distinct reddish color. Accordingly,
202 surface area as well as surface relaxivity are dominated by the clay and Fe-bearing minerals and should be
203 significantly different than for the BH5-2 sample.

204 The experimental methods used in this study include digital image analysis (DIA) based upon micro
205 computed tomography (μ -CT), mercury intrusion porosimetry (MIP), nuclear magnetic resonance (NMR),
206 and spectral induced polarization (SIP).

207

208 For this study, a nanotom S 180 X-ray μ -CT equipment (GE sensing and inspection technologies) has been
209 used. The sample size for μ -CT scanning is 2mm diameter and 4 mm length. For pore network separation, a
210 combination of manual thresholding and watershed algorithms has been applied to achieve the qualitatively
211 best separated pore space. Additionally, separation results have been cross checked with the images of
212 scanning electrode microscopy (SEM). More details on the DIA workflow can be found in Halisch et al.
213 (2016). The DIA of the 3-D μ -CT data sets provide for each individual pore the volume and the pore radius
214 of the largest sphere that can be placed inside this pore (maximum inscribed sphere method, e.g. Silin and
215 Patzek, 2006) as indicated by the blue circles in Figure 1. Note that Figure 1 displays a 2-D slice with
216 circles. The DIA is performed in 3-D volumes and provides spheres. The resulting equivalent pore radius is
217 referred to as pore body radius r_b . Though the true extent of the pore is not caught properly, the derived r_b
218 from DIA is a good estimate of the average radius. Adding up the pore volumes starting with the lowest
219 pore radius yields the cumulative volume fraction of pores V_c (Eq. (1)) as a function of the pore body radius
220 r_b . The μ -CT method can only resolve the part of the pore space with pore sizes larger than the spatial
221 resolution of the 3D image. Considering a voxel size of 1.75 μm of the 3D data set, and a minimum
222 extension of pores of two voxels in one direction, which can be separated by the algorithm, a minimum
223 pore size of 3.5 μm (or minimum pore radius of 1.75 μm) has to be regarded, as for this study, the CT
224 resolution limit is 1.75 μm . Therefore, the pore volume determined by μ -CT does not take into account the
225 pore space with radii smaller than 1.75 μm .

226

227 The MIP experiments have been conducted with the PASCAL 140/440 instrument from Thermo Fisher
228 (Mancuso et al., 2012), which covers a pressure range between 0.015 MPa and 400 MPa corresponding to a
229 pore throat radius range from (at best) 1.8 nm to 55 μm . The samples have been evacuated before the MIP
230 experiment. Starting with low pressure, the pores with larger pore throats are filled with mercury. While
231 increasing the pressure, the pores with smaller throats are filled. Reaching a certain pressure level P_c , a

232 cumulative volume of mercury (V_{Hg}) has intruded into the sample that corresponds to the pore volume
233 being accessible by pore throats radii larger or equal r_t according to Eq. (2).

234

235 The NMR experiments have been performed with a Magritek Rock Core Analyzer equipment operating at a
236 Larmor frequency of 2 MHz at room temperature ($\sim 20^\circ\text{C}$) and ambient pressure. After drying at 105°C for
237 more than 24 hours in vacuum, the samples have been fully saturated with tap water with a conductivity of
238 about 25 mS/m. NMR measurements can be calibrated to get the porosity of the sample. The early time
239 decay signal corresponds to the total water content. The range of resolved pore radii depends on the used
240 value of surface relaxivity. The amplitude b attributed to an individual relaxation time T_2 is related to the
241 volume fraction of pores with the respective pore radius. Considering the larger pores, the resulting radius
242 corresponds to r_b . The smaller pore throats with lower volume yield a lower signal at shorter relaxation
243 times. The cumulative volume fraction of pores V_c is determined by adding up the individual b values
244 starting from the smallest relaxation time and normalizing to the total sum of all b values.

245

246 Complex conductivity spectra were recorded using a four-electrode sample holder as described by Schleifer
247 et al. (2002). The spectra were acquired with the impedance spectrometer ZEL-SIP04 (Zimmerman et al.,
248 2008) in a frequency range between 0.002 Hz and 45 kHz at a constant temperature of about 20°C .
249 Considering that the complex conductivity spectra are affected by electromagnetic coupling effects, ~~or~~
250 ~~other~~ Maxwell Wagner relaxation and dielectric effects at higher frequencies and by a lower signal to noise
251 ratio for lower frequencies, we focus on the frequency range between 0.01 Hz and 100 Hz. The samples
252 were fully saturated with a sodium-chloride solution with a conductivity of 100 mS/m. At least two
253 measurements were performed for each sample to verify the repeatability. Considering the limited
254 frequency interval, the SIP method solely resolves a range of pore radii that depends on the diffusion
255 coefficient. Hence, using $D_{(+)} = 3.8 \times 10^{-12} \text{ m}^2/\text{s}$ in Eq. (6), we get a range of pore radii between 0.1 μm and
256 10 μm . Smaller pore sizes are hidden by Maxwell Wagner relaxation and dielectric effects that are not
257 easily related to pore geometry.

258

259 4 Results

260 4.1 Petrophysical properties

261 Figure 2 (A and C) gives 2-D impressions of the pore system of the Bentheimer sandstone sample. The
262 pore space in general is very well connected, featuring many large and open pores (Fig.2, A & C, blue
263 arrows) and can be described as a classical pore body – pore throat – pore body system. Small pores are
264 mostly found within the clayey agglomerations, which act as (macro) pore filling material (Fig.2, A & C,

265 red arrows) and which are homogeneously distributed throughout the sample material. Figure 2 E gives an
 266 impression of the 3-D pore distribution of this sandstone, derived by μ -CT image processing. This
 267 favorable structure is directly reflected by the petrophysical properties of this sandstone. The sample
 268 investigated in our study is characterized by a porosity of 0.238 measured by MIP, a gas-permeability of
 269 $4.25 \times 10^{-13} \text{ m}^2$ determined by steady-state permeameter (manufactured by Westphal Präzisionstechnik) with
 270 a Fancher-type core holder using nitrogen as the flowing fluid, and a specific surface area of $0.3 \text{ m}^2/\text{g}$
 271 determined by Nitrogen adsorption method.

272 Figure 2 (B and D) shows the pore space of the Röttbacher sandstone sample from 2-D imaging techniques.
 273 Though the (large) pore space is similar structured as it is for the Bentheimer (pore body-throat-body
 274 system, Fig. 2, B & D, blue arrows), it is generally reduced (cemented) by clay minerals and features a
 275 significantly higher amount of small pores within (Fig. 2, B & D, red arrows). Accordingly, pore space
 276 related petrophysical properties classify a more compact rock, which is supported by the 3-D pore
 277 distribution, derived by μ -CT image processing (Fig. 2, F). The sample used for this study features a
 278 porosity of 0.166 measured by MIP, which is lower than for the Bentheimer sandstone. The gas-
 279 permeability is $3.45 \times 10^{-14} \text{ m}^2$, which is less than 10 % of the value determined for the Bentheimer
 280 sandstone. The specific surface area has been measured with $1.98 \text{ m}^2/\text{g}$ and is hence nearly seven times
 281 larger than for sample BH5-2, clearly underlining the impact of the clay content. The petrophysical
 282 parameters for both samples are compiled in Table 1, whereas results from X-ray fluorescence analysis are
 283 summarized in Table 2, regarding the most important chemical components of both sandstones that have
 284 been used for this study.

285 4.2 Pore volume fraction

286 We applied the methods μ -CT, MIP, NMR, and SIP to get insight into the pore radius distribution of the
 287 Bentheimer sandstone sample BH5-2. Figure 3 displays the resolved porosity ϕ_r as a function of pore radius
 288 for μ -CT and MIP data. The cumulative pore volume while progressing from larger to smaller pores $V(>r)$
 289 is normalized to the total volume of the sample V_s and results in the resolved porosity

$$290 \quad \phi_r = \frac{V(>r)}{V_s}, \quad (7)$$

291 which reaches the true porosity ϕ as threshold value for r approaching zero.

292 As shown in Figure 3, the μ -CT method identifies the largest pores with pore body radii of about $100 \mu\text{m}$.
 293 The resolved porosity ϕ_r reaches a value of 0.184 at the limit of resolution of the μ -CT method ($r_b=1.75$
 294 μm). The nearly horizontal curve progression for $r < 17 \mu\text{m}$ indicates that effectively no significant volume
 295 of pores with radii lower than $17 \mu\text{m}$ were detected or quantified by μ -CT and DIA, respectively.
 296 Accordingly, only μ -CT data for $r > 17 \mu\text{m}$ will be taken into account for further analysis.

297 The MIP identifies the largest pore throats with a radius of about 30 μm . Reaching the limit of resolution of
298 the MIP, the resolved porosity approaches asymptotically the threshold value of 0.238. Though both
299 methods $\mu\text{-CT}$ and MIP yield the pore radius without any adjustable scaling factor, we observe differences
300 between the two curves $\phi_r(r)$ in Figure 3.

301 The Röttbacher sample was scanned with resolution 1.5 μm by $\mu\text{-CT}$. As shown in Figure 7, the $\mu\text{-CT}$
302 method identifies the largest pores with pore body radii of about 90 μm . The resolved porosity ϕ_r reaches a
303 value of 0.106 at the limit of resolution of the $\mu\text{-CT}$ method ($r_b=1.5 \mu\text{m}$). As observed for the Bentheimer
304 sandstone, the nearly horizontal curve progression for $r < 10 \mu\text{m}$ indicates that no significant volume of
305 pores with radii lower than 10 μm were detected or quantified by $\mu\text{-CT}$ and DIA, respectively. Accordingly,
306 only $\mu\text{-CT}$ data for $r > 10 \mu\text{m}$ will be taken into account for further analysis.

307 **4.3 Pore radius distribution**

308 The description and quantification of the pore space in three dimensions requires morphological parameters
309 such as length, width, and thickness of individual pore segments. The parameters are extracted by image
310 analysis software from 3-D $\mu\text{-CT}$ data. We determined the pore length (maximum length of Feret
311 distribution), pore width (minimum width of Feret distribution), and the equivalent diameter of the
312 analyzed pore segment that corresponds to the spherical diameter with equal voxel volume (Schmitt et al.,
313 2016). The minima, maxima, and mean values of the geometrical parameters derived from $\mu\text{-CT}$ data of the
314 two samples are compiled in Table 3.

315 The procedures described above result in an individual curve displaying the logarithm of V_c versus the
316 logarithm of the pore radius for each method.

317 For Bentheimer sandstone, applying the transformation in Eq. (3) for the MIP data and assuming a true
318 porosity of 0.238, the cumulative volume fraction of pores V_c can be displayed as a function of pore radius
319 as shown in Figure 4. The MIP curve gets a fixed position in the plot of Figure 4 without the need for any
320 scaling. It covers a wide range of pore radii between 0.0018 and 44.7 μm .

321 The curves resulting from other methods have to be adjusted considering the limits of the range of pore
322 radii. The maximum of the $\mu\text{-CT}$ curve corresponds to $V_c = 1$ because no larger pore size has been detected
323 by other methods. The maximum resolved porosity of the sample as detected by MIP reaches 0.238. The
324 porosity determined by $\mu\text{-CT}$ reaches only 0.184 (Figure 3). This value corresponds to a fraction of 0.773
325 of the porosity determined by MIP. Therefore, the minimum of the $\mu\text{-CT}$ curve at the pore radius of 17 μm
326 has to be adjusted at $V_c = 1 - 0.773 = 0.227$, because this fraction of pore volume is related to pore radii
327 smaller than 17 μm . The shift of the $\mu\text{-CT}$ curve to larger pore radii in comparison with MIP is observed in
328 this plot, too.

329 The T_2 relaxation time distribution of sample BH5-2 is plotted in Figure 5. It indicates a distinct maximum
330 at a relaxation time of 330 ms and two weaker maxima at lower relaxation times. The T_2 relaxation time

331 distribution is transformed into a curve showing the cumulative intensity as a function of T_2 . The total
332 intensity is attributed to the total pore volume. The volume fraction V_c corresponds to the ratio of
333 cumulative intensity to total intensity. In order to get the curve V_c as a function of pore radius, the
334 relaxation time T_2 has to be transformed into a pore radius using the surface relaxivity ρ as scaling factor in
335 Eq. (5). Since both μ -CT and NMR method are sensitive to the pore body radius, we expect a similar $V_c - r$
336 - curve in the overlapping range of pore radii. Assuming a coincidence of the two curves at $V_c = 0.5$, the
337 surface relaxivity is adjusted at $\rho = 54 \mu\text{m/s}$.

338 **The complex conductivity spectra of the Bentheimer sample are displayed in Figure 6.** Considering the
339 frequency range between 0.01 and 100 Hz and $D_{(+)} = 3.8 \times 10^{-12} \text{ m}^2/\text{s}$, the relaxation time distribution
340 derived from SIP is attributed to a restricted range of pore radii between 0.1 μm and 10 μm . Assuming that
341 the polarization signals originate from the pore throats, a similarity of pores size distributions resulting
342 from MIP and SIP can be expected. It should be noted that MIP provides the distribution for a wider range
343 of pore radii. Therefore, we adjust the value of V_c at the maximum radius of the SIP to the corresponding
344 value for the MIP curve.

345 **As shown in Figure 7 for Röttbacher sandstone,** the MIP identifies the largest pore throats with a radius of
346 about 50 μm . Reaching the limit of resolution of MIP, the resolved porosity gets the value of 0.166.
347 Applying the transformation in Eq. (3) on the MIP data and assuming a true porosity of 0.166, the
348 cumulative volume fraction of pores V_c is displayed as a function of pore radius as shown in Figure 8.

349 We suppose that the MIP method detects the whole pore volume, a porosity of 0.106 recognized by μ -CT
350 corresponds to 63.9% of the total pore volume. Therefore, the minimum of the μ -CT curve at the pore
351 radius of 10 μm has to be adjusted at $V_c = 1 - 0.639 = 0.361$, because this fraction of pore volume is related
352 to pore radii smaller than 10 μm .

353 The T_2 relaxation time distribution of sample RÖ10B is plotted in Figure 5. It indicates a distinct maximum
354 at a relaxation time of 170 ms. Non-vanishing signals are observed at relaxation times below 0.1 ms. This is
355 an indication of the existence of very small pores in the Röttbacher sandstone.

356 The position of the NMR curve in the plot of Figure 8 depends on the surface relaxivity ρ . A coincidence
357 with the μ -CT curve at $V_c = 0.5$ requires a surface relaxivity of $\rho = 237 \mu\text{m/s}$ for adjusting the NMR curve.

358 The complex conductivity spectra of the Röttbacher sample are displayed in Figure 6. The processing of the
359 spectra according to the described algorithm results in the $V_c - r$ - curve as shown in Figure 8. The SIP
360 curve is fixed at the value $V_c = 0.9$ that has been determined by MIP for the maximum pore radius resolved
361 by SIP ($r_t = 10 \mu\text{m}$).

362

363 5 Discussion

364 Previous studies have compared the $V_c - r$ curves resulting from different methods (e.g. Zhang and Weller,
365 2014; Zhang et al., 2017; Ding et al., 2017). The slope of the curves was used to get a fractal dimension. It
366 became obvious that the distribution curves indicate remarkable differences that are caused by the physical
367 principles of the used methods. The methods differ with regard to their limits of resolution. The effective
368 resolution of μ -CT is limited by the voxel size. Larger pores can be easily detected. Nevertheless, even
369 though the derived image (voxel) resolution is quite high (1.75 μm), both sandstone data sets feature no
370 significant volume of pore radii smaller than 10 μm (BH-5) and 17 μm (RÖ-10), respectively. We assume
371 that this is caused by a complex and sensitive mixture of issues about image resolution, image quality
372 (phase contrast), reliability of the watershed-algorithm concerning the separation of individual pores, and
373 hence of the complexity of the pore structure of small pores. The MIP yields the widest range of pore radii.
374 The pore radius is directly related to the pressure. A similarly wide range of pore radii can be resolved by
375 NMR. However, the transformation of the NMR transversal relaxation time into a pore radius requires the
376 surface relaxivity as scaling factor. In a similar way, the transformation of the electrical relaxation time
377 resulting from SIP into a pore radius is based on a scaling factor that depends on the diffusion coefficient.
378 Only a restricted range of pore radii can be resolved by SIP.

379 Beside the range of pore radii, the geometrical extent of the pore radius differs among the methods. μ -CT
380 enables a geometrical description of the individual pore space considering the shape of the pore. The pore
381 radius can be determined in different ways. We use the average pore radius as an equivalent for the pore
382 body radius r_b . MIP is sensitive to the pore throat radius r_t that enables the access to larger pores behind the
383 throat. The NMR relaxation time is related the pore body radius r_b . We assume that the IP signals are
384 caused by the ion-selected active zones in the narrow pores that are comparable with the pore throats.

385 Regarding the differences of the methods, we present an approach that combines the curves to get more
386 information on the pore space. Considering the two kinds of pore radii r_b and r_t , we use first μ -CT and
387 NMR to generate a combined curve displaying V_c as a function of r_b . In the next step, we link the curves
388 resulting from MIP and SIP to get a curve showing V_c as a function of the pore throat radius r_t .

389 It is fundamental that the total pore volume (or total porosity) has to be known. The cumulative pore
390 volume fraction should only consider the pore volume that is resolved in the regarded range of pore radii.
391 Considering the resolution of μ -CT, only the pore space with radii larger than the voxel size is determined.
392 The cumulative pore volume fraction at the limit of resolution has to be adjusted to the non-resolved pore
393 volume. In this way, the μ -CT curve gets a fixed position in the $V_c - r$ plot. Regarding NMR, the relaxation
394 time T_2 has to be transformed into a pore radius according to Eq. (5). The application of Eq. (5) requires the
395 knowledge of the surface relaxivity ρ , which is the necessary scaling factor that causes a shift of the $V_c - r$
396 curve along the axis of pore radius. Since NMR method is sensitive to the pore body radius, we expect a
397 similar $V_c - r$ curve for NMR and μ -CT in the overlapping range of pore radii. The NMR curve is shifted

398 along the axis of pore radii until a good agreement between the two curves is reached. This procedure
399 enables the adjustment of the surface relaxivity.

400 MIP is used to generate the curve displaying V_c as a function of r_t over a wide range of pore radii. The SIP
401 curve is fixed at the MIP curve considering the coincidence at the largest pore radius resolved by SIP.

402 The two curves representing V_c as a function of both r_b and r_t are displayed in a double logarithmic plot.
403 The horizontal shift of the two graphs represents the ratio r_b/r_t . Additionally, the slope of the curves is
404 related to the fractal dimension.

405 The proposed approach in this study results in two pore size distribution curves for the two samples, which
406 are in good accordance to the general pore space structures as described in section 3 and as visualized in
407 Figure 2 (A to F). The first curve combines the distributions resulting from μ -CT and NMR. The μ -CT data
408 provide a pore radius, which is regarded as pore body radius, without any scaling. The scaling of the NMR-
409 curve provides an estimate of the surface relaxivity. The surface relaxivity of the Bentheimer sample
410 reaches 54 $\mu\text{m/s}$, the corresponding value of the Röttbacher sample is with 237 $\mu\text{m/s}$ much higher. The
411 higher surface relaxivity in comparison with the Bentheimer sample is clearly justified considering the
412 larger specific surface area (Table 1) and the significantly higher content of clay and iron-bearing minerals
413 as indicated in Table 2 (e.g. Keating and Knight, 2010).

414 The two cumulative pore volume distribution curves for the Röttbacher sample (Figure 8) indicate over the
415 wide range of pore radii a parallel progression with consistently higher values for the pore body radius (μ -
416 CT and NMR) in comparison with the pore throat radius (MIP). The horizontal distance of the two curves
417 yields the ratio r_b/r_t . Regarding the median pore radii at $V_c = 0.5$, a ratio $r_b/r_t = 9.13$ is determined.
418 Considering smaller pores, a ratio $r_b/r_t = 12.15$ is indicated at $V_c = 0.05$.

419 The parallelism of the pore volume distribution curve is less developed for the Bentheimer sample (Figure
420 4). We observe a clear distance of the two curves in the range of larger pore radii. Regarding the median
421 pore radii at $V_c = 0.5$, a ratio $r_b/r_t = 2.57$ is determined. For $V_c < 0.2$, the slope of the curves decreases and
422 smaller distances between the curves are observed. The NMR curve in Figure 4 indicates for $V_c > 0.08$
423 larger pore radii in comparison with the MIP curve and confirms the relationship $r_b > r_t$. The reverse
424 behavior in the interval $0.1 \mu\text{m} < r < 0.6 \mu\text{m}$ is possibly caused by the low volume fraction (3%) attributed
425 to this range of pore radii. It can be expected that the small amount of water in the small pores causes only
426 weak signals in the NMR relaxometry.

427 Beside the distances between the curves the individual slopes are regarded. The slope (s) of the curve \log
428 (V_c) versus \log (r) is related to the fractal dimension D of the pore volume ($D = 3 - s$) (Zhang and Weller,
429 2014). We observe a varying slope in the investigated range of pore radii for the Bentheimer sample. The
430 only range of more or less constant slope, which extends from pore radius $0.1 \mu\text{m}$ to $10 \mu\text{m}$, corresponds to
431 a fractal dimension $D_{MIP} = 2.678$ for MIP, $D_{NMR} = 2.776$ for NMR, and $D_{SIP} = 2.618$ for SIP.

432 The whole curves of the four methods are non-linear and indicate non-fractal behavior. A Maximum
433 Likelihood Estimator approach (MLE) might be relevant to extract the underlying scaling parameters
434 (Rizzo et al., 2017). For example, in the case of the NMR curve of Bentheimer sandstone, the fitting of all
435 data using the MLE reveals that the log-normal distribution is the most likely distribution with the
436 estimated parameters $\mu = 3.43 \mu\text{m}$ and $\sigma = 0.82 \mu\text{m}$. These two scaling parameters are the logarithmic mean
437 and logarithmic standard deviation of the pore radius, respectively. We recognize that the resulting mean
438 radius reaches half value of the effective hydraulic radius ($r_{eff} = 6.97 \mu\text{m}$).

439 We observe a constant slope of the NMR curve for the Röttbacher sample (Figure 8) in the interval
440 $0.01 \mu\text{m} < r_b < 100 \mu\text{m}$. A similar slope is observed for the MIP curve in the interval $0.01 \mu\text{m} < r_t < 10 \mu\text{m}$.
441 Considering the overlapping pore throat radii range between $0.1 \mu\text{m}$ and $10 \mu\text{m}$, a fractal dimension D with
442 values of 2.640 for MIP, and 2.661 for NMR has been determined. The slightly higher slope of the SIP
443 curve results in a lower value of fractal dimension of $D = 2.533$.

444 Our approach enables the integration of SIP in the determination of a pore throat size distribution.
445 Considering the limited frequency range, only a limited range of pore throat radii can be reflected. Using a
446 fixed diffusion coefficient $D_{(+)} = 3.8 \times 10^{-12} \text{ m}^2/\text{s}$, a range of pore throat radii between $0.1 \mu\text{m}$ and $10 \mu\text{m}$ is
447 resolved. The SIP curve is linked to the MIP curve at $r = 10 \mu\text{m}$. An extension to lower pore radii would
448 require the integration of higher frequencies. The removal of electromagnetic coupling effects can be one
449 first step to improve the reliability of complex conductivity spectra for frequencies larger than 100 Hz, but
450 it should be regarded that even small pore sizes are hidden by Maxwell Wagner and dielectric relaxation.

451 The proposed procedure results in a fair agreement between SIP and MIP curves in the overlapping range
452 of pore throat radius for both the Bentheimer and the Röttbacher sample. In comparison with MIP, a slight
453 overestimation of V_c is observed for larger pore throat radii and a underestimation for lower pore throat
454 radii. Considering the two samples of the presented study, the assumption of a constant diffusion
455 coefficient seems to be justified. Though alternative kernels have not been tested, our study confirms that
456 the Debye decomposition provides a relaxation time distribution of complex conductivity spectra that can
457 be transformed in a pore throat size distribution comparable with the resulting curves from MIP. Regarding
458 the discussion on the most relevant parameter that controls the relaxation time, our assumption that the pore
459 throat radius is related to the relaxation time is supported by the results.

460 The investigations by μ -CT, MIP, NMR, and SIP on the sandstone samples have been done in the
461 laboratory. μ -Ct and MIP are methods that can only be applied on rock samples. The potential of these
462 methods to derive pore size distributions is well acknowledged. NMR and SIP are methods that can also be
463 performed in boreholes or as field survey. The NMR method has been successfully applied in permeability
464 prediction at the field scale. A variety of permeability prediction models based on SIP parameters has been
465 proposed based on laboratory investigations (e.g. Robinson et al., 2018). First tests have demonstrated their
466 applicability in the field. Most permeability models consider pore size and porosity as the most important

467 parameters. The evaluation of pore sizes of sediments at the field scale is a challenging task for geophysical
468 methods. Our laboratory study has demonstrated the potential of SIP in identifying a pore size distribution.
469 Further investigations with larger sets of samples have to be done to improve the proposed procedure
470 before the pore size distribution can be extracted from high quality complex conductivity field spectra.
471

472 **6 Conclusions**

473 Pore radii distributions have been determined by different methods (μ -CT, MIP, NMR, and SIP) for two
474 sandstone samples. The curves presenting the cumulative distribution of pore volume V_c as a function of
475 pore size have proved to be a suitable tool for comparison. It becomes obvious that the distribution curves
476 indicate remarkable differences that are based on the physical principles of the used methods. The methods
477 differ with regard to their limits of resolution. The effective resolution of μ -CT is limited by the voxel size
478 (1.75 μm). Larger pores can be easily detected, whereas quantification of small pores and volumes of pores
479 with small radii is severely affected by the image quality and the image processing algorithms. The MIP
480 yields the widest range of pore radii. The pore radii are directly related to the pressure interval. A similar
481 wide range of pore radii can be achieved by NMR. However, the transformation of the NMR transversal
482 relaxation time into a pore radius requires the surface relaxivity as scaling factor. In a similar way, the
483 transformation of the electrical relaxation time resulting from SIP into a pore radius is based on a scaling
484 factor that depends on the diffusion coefficient. Only a restricted range of pore radii (0.1 μm to 10 μm) can
485 be resolved by SIP.

486 Beside the range of pore radii, the geometrical extent of the pore radius differs among the methods. μ -CT
487 enables a geometrical description of the individual pore space considering the shape of the pore. The pore
488 radius can be determined in different ways. We use the average pore radius as an equivalent for the pore
489 body radius r_b . MIP is sensitive to the pore throat radius r_t that enables the access to larger pores behind the
490 throat. The NMR relaxation time is related to an average pore body radius r_b . We assume that the IP signals
491 are caused by the ion-selected active zones in the narrow pores that are comparable with the pore throats.

492 Considering the two kinds of pore radii r_b and r_t , we use μ -CT and NMR to generate a combined curve
493 displaying V_c as a function of r_b . A good agreement between the two curves is achieved if they coincide at
494 $V_c = 0.5$. This condition is used to determine the surface relaxivity, which is in good accordance to the
495 investigated surface area and mineralogy of the sample materials. MIP is used to generate the curve
496 displaying V_c as a function of r_t over a wide range of pore radii. The SIP curve is fixed at the MIP curve
497 considering the coincidence at the largest pore radius resulting from SIP.

498 The two curves representing V_c as a function of both r_b and r_t are displayed in a double logarithmic plot.
499 The horizontal shift of the two graphs represents the ratio r_b/r_t . Additionally, the slope of the curves is
500 related to the fractal dimension.

501 The investigations on the samples demonstrate that the porosity increases using a method with a higher
502 resolution. Both porosity and pore volume are parameters that depend on the resolution. The fractal
503 dimension describes the size of geometric objects as a function of resolution. Therefore, the knowledge of
504 fractal behavior enables upscaling and downscaling of geometric quantities. The Bentheimer sandstone
505 sample is characterized by a ratio $r_b/r_t = 2.57$ for the larger pores. A fractal behavior is observed in the
506 range of pore radii between 0.1 μm and 10 μm with an average $D = 2.69$ determined for the pore volume by
507 MIP, NMR, and SIP. The Röttbacher sandstone sample indicates with $r_b/r_t = 9.13$ a larger ratio between
508 pore body radius and pore throat in comparison with the Bentheimer sample. An average fractal dimension
509 of $D = 2.61$ is determined for the Röttbacher sample.

510 **Acknowledgements**

511 The authors thank Sven Nordsiek (University Bayreuth) for the Debye decomposition of the SIP data,
512 Dietmar Meinel (BAM, Berlin) for supporting the CT analysis, Carsten Prinz (BAM, Berlin) for providing
513 the MIP data, and Mike Müller-Petke as well as Raphael Dlugosch (both LIAG) for the acquisition of the
514 NMR spectra for this study. Dr. Zeyu Zhang thanks Bundesanstalt für Materialforschung und –prüfung
515 (BAM, Berlin) for the Adolf-Martens-Fellowship that enabled his stay in Germany for the experimental
516 research.

517 **References**

518 Avnir, D., and Jaroniec, M.: An isotherm equation for adsorption on fractal surfaces of heterogeneous
519 porous materials, *Langmuir*, 5, 6, 1412–1433, 1989.

520 Avnir, D., Farin, D., and Pfeifer, P.: Molecular fractal surfaces, *Nature*, 308, 261-263, 1984.

521 Behroozmand, A., Keating, K., and Auken, E.: A review of the principles and applications of the NMR
522 technique for near-surface characterization, *Surv Geophys*, 36, 27–85, doi: 10.1007/s10712-014-9304-0,
523 2015.

524 Binley, A., Slater, L. D., Fukees, M., and Cassiani, G.: Relationship between spectral induced polarization
525 and hydraulic poroproperties of saturated and unsaturated sandstone, *Water Resources Research*, 41, W12417,
526 doi:10.1029/2005WR004202 , 2005.

527 Ding, Y., Weller, A., Zhang, Z., and Kassab, M.: Fractal dimension of pore space in carbonate samples
528 from Tushka Area (Egypt), *Arabian Journal of Geosciences*, 10, 388, doi: 10.1007/s12517-017-3173-z,
529 2017.

- 530 Dubelaar, W. C., and Nijland, T. G.: The Bentheim Sandstone: geology, petrophysics, varieties and its use
531 as dimension stone, in: Engineering Geology for Society and Territory, 8, Lollino, G., Giordan, D.,
532 Marunteanu, C., Christaras, B., Yoshinori, I., and Margottini, C. (Eds.), Springer International Publishing,
533 Switzerland, 557-563, 2015.
- 534 Florsch, N., Revil, A., and Camerlynck, C.: Inversion of generalized relaxation time distributions with
535 optimized sampling parameter, *Journal of Applied Geophysics*, 109, 119-132, 2014.
- 536 Gaboreau, S., Robinet, J. C., Tournassat, C., and Savoye, S.: Diffuse transport in clay media: μm to nm
537 scale characterization of pore space and mineral spatial organization: International Meeting Clays in
538 Natural and Engineered Barriers for Radioactive Waste Confinement, Montpellier, France, October 2012,
539 hal-00705345, 2012.
- 540 Halisch, M., Schmitt, M., and Fernandes, C. P.: Pore Shapes and Pore Geometry of Reservoirs Rocks from
541 $\mu\text{-CT}$ Imaging and Digital Image Analysis, in: Proceedings of the Annual Symposium of the SCA 2016,
542 Snowmass, Colorado, USA, 21-26 August 2016, SCA2016-093, 2016.
- 543 Halisch, M., Steeb, H., Henkel, S., and Krawczyk, C. M.: Pore-Scale tomography and imaging:
544 applications, techniques and recommended practice, *Solid Earth Special Issue, Solid Earth*, 7, 1141-1143,
545 doi:10.5194/se-7-1-2016, 2016.
- 546 Keating, K., and Knight, R.: A laboratory study of the effect of Fe(II)-bearing minerals on nuclear magnetic
547 resonance (NMR) relaxation measurements, *Geophysics*, 75, 3, F71–F82, 2010.
- 548 Keller, L. M., Holzer, L., Wepf, R., Gasser, P., Münch, B., and Marschall, P.: On the application of focused
549 ion beam nanotomography in characterizing the 3D pore space geometry of Opalinus clay, *Physics and
550 Chemistry of the Earth*, 36, 1539-1544, doi:10.1016/j.pce.2011.07.010, 2011.
- 551 Kelokaski, M., Siitari-Kauppi, M., Sardini, P., Mori, A., and Hellmuth, K.H.: Characterisation of pore
552 space geometry by ^{14}C -PMMA impregnation-development work for in situ studies, *Journal of Geochemical
553 Exploration*, 90, 45-52, doi:10.1016/j.gexplo.2005.09.005, 2005.
- 554 Kleinberg, R. L.: Utility of NMR T_2 distributions, connection with capillary pressure, clay effect, and
555 determination of the surface relaxivity parameter ρ_2 , *Magnetic Resonance Imaging*, 14, 761–767, 1996.
- 556 Kruschwitz, S., Prinz C., and Zimathies A.: Study into the correlation of dominant pore throat size and SIP
557 relaxation frequency, *Journal of Applied Geophysics*, 135, 375-386, 2016.

- 558 Leroy, P., Revil, A., Kemna, A., Cosenza, P., and Gorbani, A.: Spectral induced polarization of water-
559 saturated packs of glass beads, *J. Colloid Interface Sci*, 321, 103-117, doi:10.1016/j.jcis.2007.12.031, 2008.
- 560 Mandelbrot, B. B.: *Fractals: form, chance, and dimension*, Freeman, San Francisco, 1977.
- 561 Mandelbrot, B. B.: *Fractal geometry of nature*, Freeman, San Francisco, 1983.
- 562 Mancuso, C., Jommi, C., and D'Onza, F. (Eds.): *Unsaturated Soils: Research and Applications*, Volume 1,
563 Springer-Verlag Berlin Heidelberg, 123-130, doi: 10.1007/978-3-642-31116-1, ISBN: 978-3-642-31115-4
564 (Print), 2012.
- 565 Mees, F., Swennen, R., van Geet, M., and Jacobs, P. (Eds.): *Applications of X-ray computed tomography*
566 *in the geosciences*, Geological Society, London, Special Publication, 215, 1, 1-6, doi:
567 10.1144/GSL.SP.2003.215.01.01, 2003.
- 568 Meyer, K., Klobes, P., and Röhl-Kuhn, B.: Certification of reference material with special emphasis on
569 porous solids, *Crystal Research and Technol.*, 32, 173-183, 1997.
- 570 Niu, Q., and Zhang, C.: Joint inversion of NMR and SIP data to estimate pore size distribution of
571 geomaterials, *Geophysical Journal International*, 212 (3), 1791-1805, doi: 10.1093/gji/ggx501, 2017.
- 572 Nordsiek, S., and Weller, A.: A new approach to fitting induced-polarization spectra, *Geophysics*, 73, 6,
573 F235-F245, doi: 10.1190/1.2987412, 2008.
- 574 Pape, H., Riepe, L., and Schopper, J. R.: A pigeon-hole model for relating permeability to specific surface,
575 *The Log Analyst*, 23, 1, 5-13, 1982.
- 576 Pape, H., Arnold J., Pechinig R., Clauser C., Talnishnikh E., Anferova S., and Blümlich B.: Permeability
577 prediction for low porosity rocks by mobile NMR, *Pure and Applied Geophysics*, 166, 1125-1163, 2009.
- 578 Peksa, A., Wolf, K., and Zitha, P.: Bentheimer sandstone revisited for experimental purposes, *Marine and*
579 *Petroleum Geology*, 67, 701-719, doi: 10.1016/j.marpetgeo.2015.06.001, 2015.
- 580 Peth, S., Horn, R., Beckmann, F., Donath, T., Fischer, J., and Smucker, A. J. M.: Three-dimensional
581 quantification of intra-aggregate pore-space features using Synchrotron-Radiation-Based
582 Microtomography, *Soil Science Society of America journal*, 72, 4, 897-907, doi: 10.2136/sssaj2007.0130,
583 2008.

584 Revil, A., and Florsch, N.: Determination of permeability from spectral induced polarization data in
585 granular media, *Geophysical Journal International*, 181, 1480-1498, 2010.

586 Revil, A., Koch, K., and Holliger, K.: Is it the grain size or the characteristic pore size that controls the
587 induced polarization relaxation time of clean sands and sandstones?, *Water Resources Research*, 48,
588 W05602, doi: 10.1029/2011WR011561, 2012.

589 Revil, A.: Effective conductivity and permittivity of unsaturated porous materials in the frequency range 1
590 mHz-1GHz, *Water Resources Research*, 49, 306-327, doi: 10.1029/2012WR012700, 2013.

591 Revil, A., Florsch, N., and Camerlynck, C.: Spectral induced polarization porosimetry, *Geophysical Journal*
592 *International*, 198, 1016-1033, doi: 10.1093/gji/ggu180, 2014.

593 Rizzo, R.E., Healy, D., and De Siena, L.: Benefits of maximum likelihood estimators for fracture attribute
594 analysis: Implications for permeability and up-scaling, *Journal of Structural Geology*, 95, 17-31, doi:
595 10.1016/j.jsg.2016.12.005, 2017.

596 Robinson, J., Slater, L., Weller, A., Keating, K., Robinson, T., Rose, C., and Parker, B.: On permeability
597 prediction from complex conductivity measurements using polarization magnitude and relaxation time,
598 *Water Resources Research*, 54, <https://doi.org/10.1002/2017WR022034>, 2018.

599 Rouquerol, J., Avnir, D., Fairbridge, D. C. W., Everett, D. H., Haynes, J. H., Pernicone, N., Ramsay, J. D.
600 F., Sing, K. S. W., and Unger, K. K.: Recommendations for the characterization of porous solids (Technical
601 Report), *Pure and Appl. Chem.*, 66, 1739-1758, 1994.

602 Schleifer, N., Weller, A., Schneider, S., and Junge, A.: Investigation of a Bronze Age plankway by spectral
603 induced polarization, *Archeological Prospection*, 9, 243–253, doi: 10.1002/arp.194, 2002.

604 Schmitt, M., Halisch, M., Müller, C., and Fernandes, C. P.: Classification and quantification of pore shapes
605 in sandstone reservoir rocks with 3-D X-ray micro-computed tomography, *Solid Earth*, 7, 285–300,
606 doi:10.5194/se-7-285-2016, 2016.

607 Schwarz, G.: A theory of the low-frequency dielectric dispersion of colloidal particles in electrolyte
608 solution, *Journal of Physical Chemistry*, 66, 2636-2642, doi: 10.1021/j100818a067, 1962.

609 Scott, J. B. T., and Barker, R. D.: Determining pore-throat size in Permo-Triassic sandstones from low-
610 frequency electrical spectroscopy, *Geophysical Research Letters*, 30, 1450, doi: 10.1029/2003GL016951.

611 Silin, D. and Patzek, T.: Pore space morphology analysis using maximal inscribed spheres, *Physica A*, 371,
612 2,336-360, doi: 10.1016/j.physa.2006.04.048, 2006.

613 Slater, L., and Lesmes, D. P.: Electric-hydraulic relationships observed for unconsolidated sediments,
614 *Water Resources Research*, 38, 10, doi:10.1029/2001WR001075, 2002.

615 Thomeer, J. H. M.: Introduction of a pore geometrical factor defined by the capillary pressure curve,
616 *Journal of Petroleum Technology*, 12(3), 73-77, 1960.

617 Washburn, E. W.: The dynamics of capillary flow, *Physical Review*, 17, 3, 273-283, 1921.

618 Weller, A., Zhang, Z., Slater, L., Kruschwitz, S., and Halisch, M.: Induced polarization and pore radius – a
619 discussion, *Geophysics*, 81, 5, D519-526, doi:10.1190/GEO2016-0135.1, 2016.

620 Weller, A., Slater, L., Binley, A., Nordsiek, S., and Xu, S.: Permeability prediction based on induced
621 polarization: Insights from measurements on sandstone and unconsolidated samples spanning a wide
622 permeability range, *Geophysics*, 80, 2, D161-D173, doi:10.1190/GEO2014-0368.1, 2015.

623 Weller, A., Nordsiek, S., and Debschütz, W.: Estimating permeability of sandstone samples by nuclear
624 magnetic resonance and spectral-induced polarization, *Geophysics*, 75, E215 – E226, doi:
625 10.1190/1.3507304, 2010.

626 Zhang, Z., Weller, A., and Kruschwitz, S.: Pore radius distribution and fractal dimension derived from
627 spectral induced polarization, *Near Surface Geophysics*, 15, 625-632, doi: 10.3997/1873-0604.2017035,
628 2017.

629 Zhang, Z., and Weller, A.: Fractal dimension of pore space geometry of an Eocene sandstone formation,
630 *Geophysics*, 79, D377-387, doi:10.1190/GEO2014-0143.1, 2014.

631 Zimmermann, E., Kemna, A., Berwix, J., Glaas, W., and Vereecken, H.: EIT measurement system with
632 high phase accuracy for the imaging of spectral induced polarization properties of soils and sediments,
633 *Measurement Science and Technology*, 19, 9, 094010, doi: 10.1088/0957-0233/19/9/094010, 2008.

634

635
636
637
638

Table 1: Petrophysical properties of the samples: porosity ϕ , permeability K , specific surface area S_m , formation factor F , dominant pore radius r_{dom} , effective pore radius r_{eff} , the ratio r_b / r_t , fractal dimensions determined from mercury intrusion porosimetry D_{MIP} , nuclear magnetic resonance D_{NMR} , and spectral induced polarization D_{SIP} , the surface relaxivity ρ , and the Diffusion coefficient $D_{(+)}$.

	unit	BH5-2	RÖ10B
Porosity (triple weighing)		0.238	0.159
Porosity (μ -CT)		0.184	0.106
Porosity (MIP)		0.238	0.166
Permeability K	m ²	4.25×10^{-13}	3.45×10^{-14}
Specific surface area	m ² /g	0.30	1.98
Formation factor F		14.3	11.3
r_{dom} (MIP)	μm	11.4	4.9
$r_{eff} = (8FK)^{0.5}$	μm	6.97	1.77
r_b / r_t		2.57	9.13
D_{MIP}		2.678	2.640
D_{NMR}		2.776	2.661
D_{SIP}		2.618	2.533
Surface relaxivity ρ	$\mu\text{m/s}$	54	237
Diffusion coefficient $D_{(+)}$	m ² /s	3.8×10^{-12}	3.8×10^{-12}

639
640

Table 2: Chemical components of the samples from X-ray Fluorescence analysis.

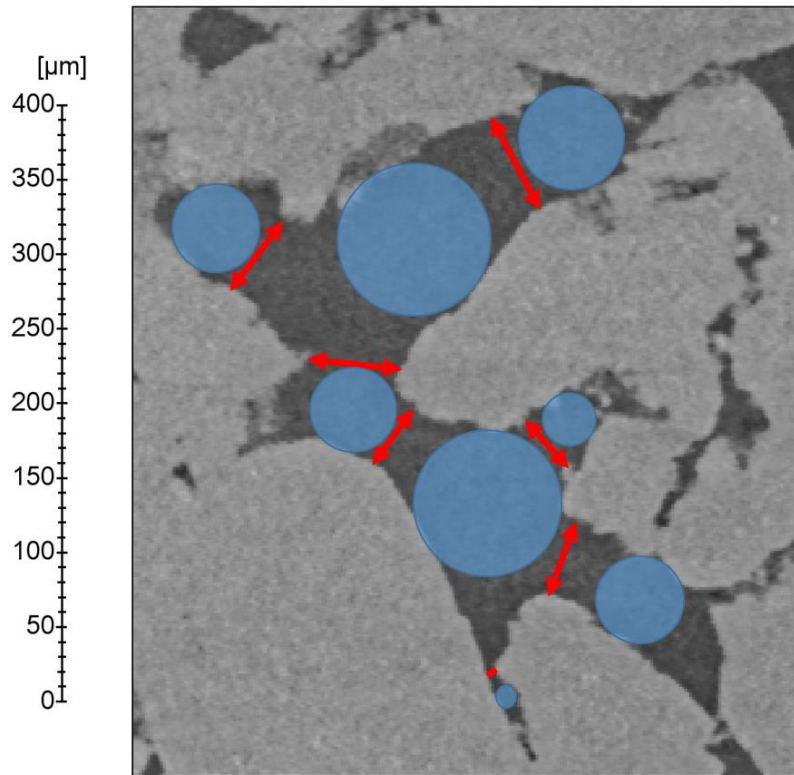
Sample	Selected chemical components from X-Ray Fluorescence [weight-%]						
	SiO ₂	TiO ₂	Al ₂ O ₃	Fe ₂ O ₃	CaO	Na ₂ O	K ₂ O
BH5-2	97.84	0.048	1.2	0.05	0.019	0.02	0.355
RÖ10B	87.06	0.356	6.06	1.07	0.225	0.13	3.679

641
642

643 **Table 3: Geometrical parameters of individual pores derived from μ -CT data of the two samples.**

descriptor	Sample					
	BH5-2			RÖ10B		
	min. [μm]	max. [μm]	mean [μm]	min. [μm]	max. [μm]	mean [μm]
equivalent pore diameter	2.17	229.1	71.56	1.86	230.4	28.95
Feret length (length 3D)	1.92	537.1	161.8	1.64	416.8	56.3
Feret Width (width 3D)	1.92	307.0	87.45	1.64	265.8	28.28
Feret breadth (breadth 3D)	1.75	379.4	114.7	1.5	354.8	37.99
pore volume [μm^3]	5.36	6294270	315069	3.38	6404830	64809

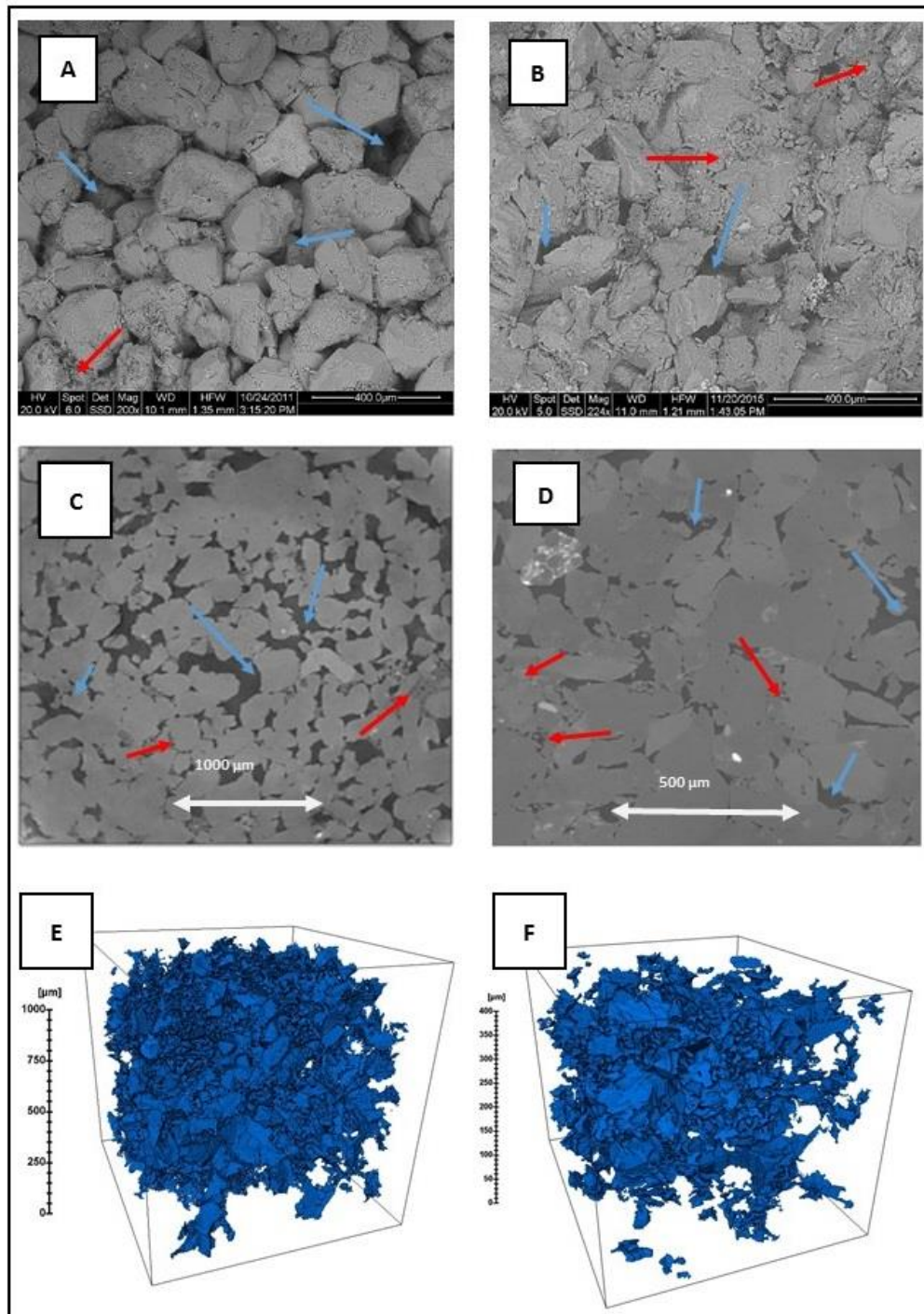
644



$\updownarrow 2x r_t$ $\bullet 2x r_b$
 determined by Hg-injection determined by CT & NMR

645
 646
 647
 648
 649

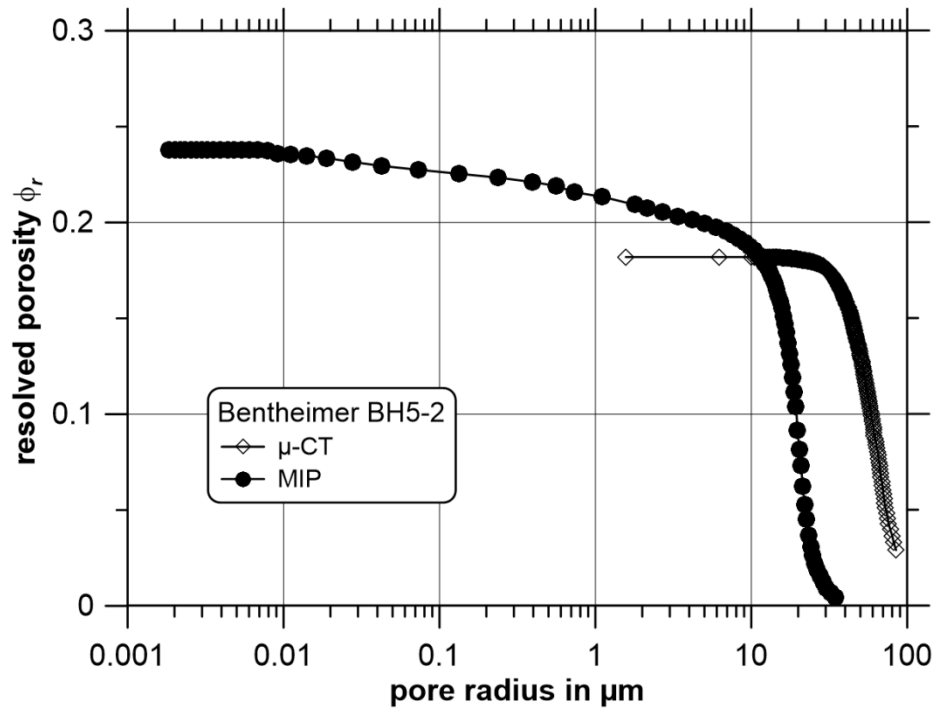
Figure 1: Zoomed in 2-D slice view of sample BH-5 in order to visualize “pore bodies” (blue circles, detected by NMR and DIA of μ -CT data) and “pore throats” (red lines with arrows, detected by MIP).



650
 651
 652
 653
 654
 655
 656

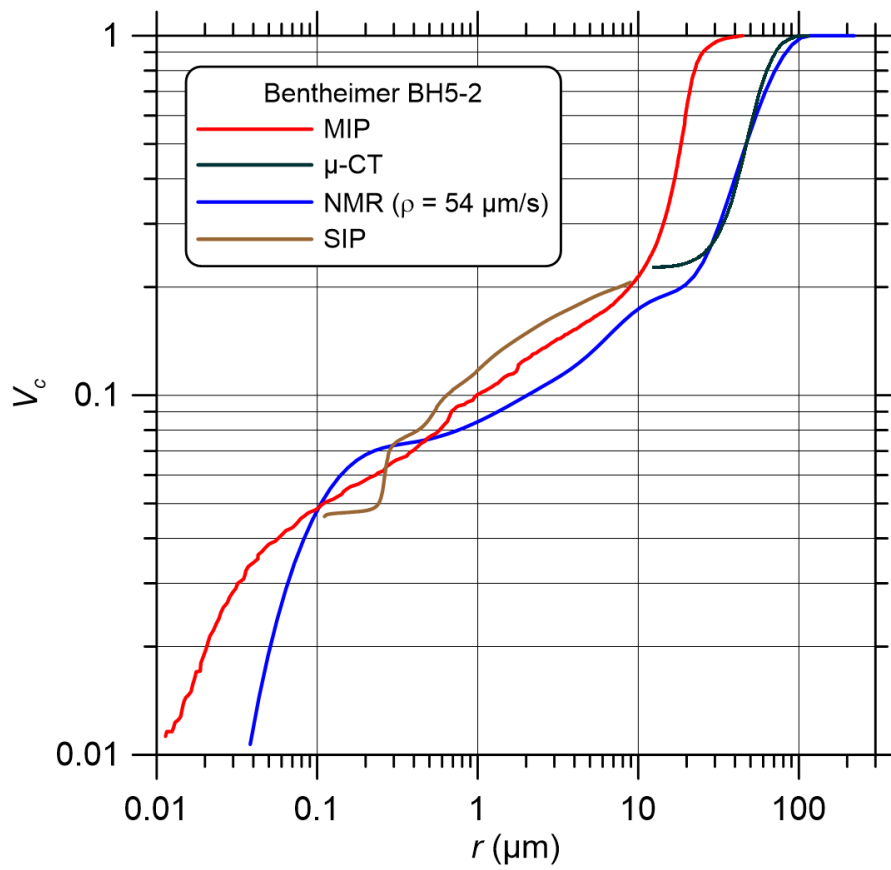
Figure 2: SEM (A) and 2D (C) and 3D (E) CT views upon the minerals and pore structure of the investigated sample of Bentheimer sandstone, and SEM (B) and 2D (D) and 3D (F) CT views upon the minerals and pore structure of the investigated sample of Röttbacher sandstone. Blue arrows indicate open pore spaces, red arrows indicate clay agglomerations and pore fillings.

657



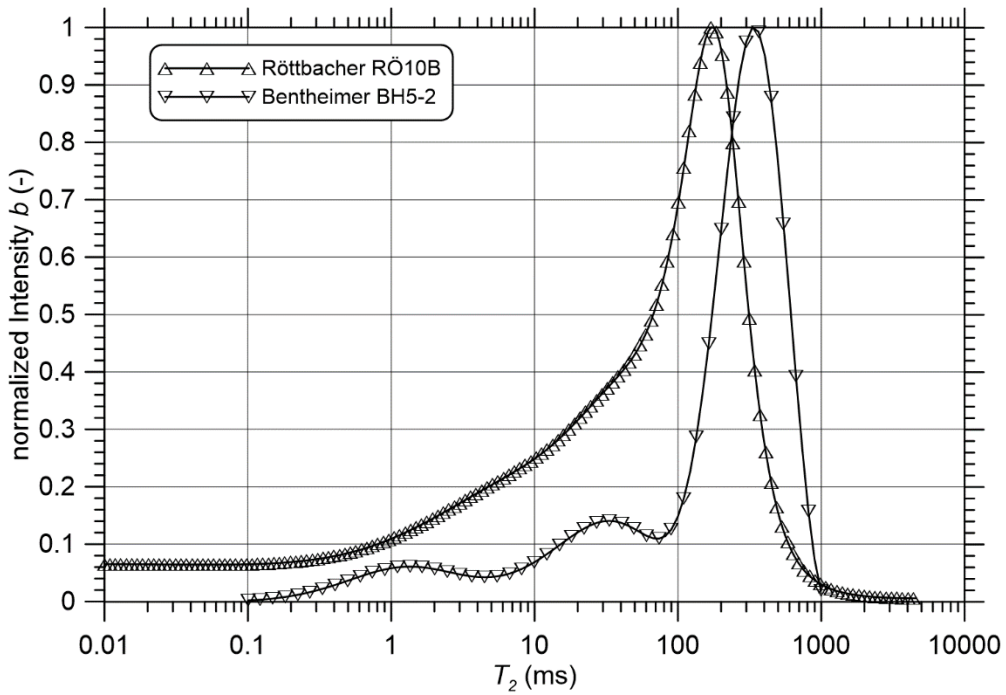
658
659
660
661

Figure 3: The recognized porosity and pore size range of Bentheimer sandstone sample BH5-2. The maximum porosity recognized by MIP is 0.238 and the maximum porosity recognized by μ -CT is 0.184.



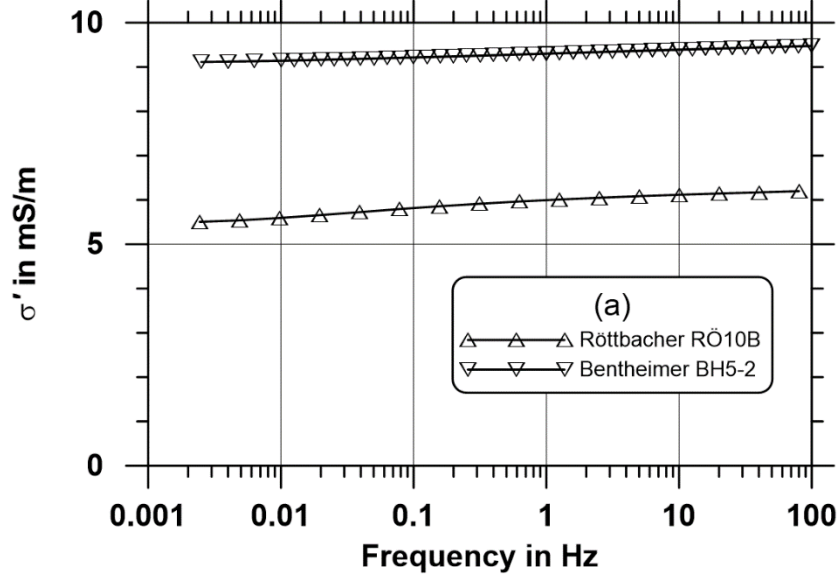
662
 663
 664
 665
 666
 667

Figure 4: The comparison of V_c - r curves determined from MIP, μ -CT, NMR and SIP for Bentheimer sandstone sample BH5-2.

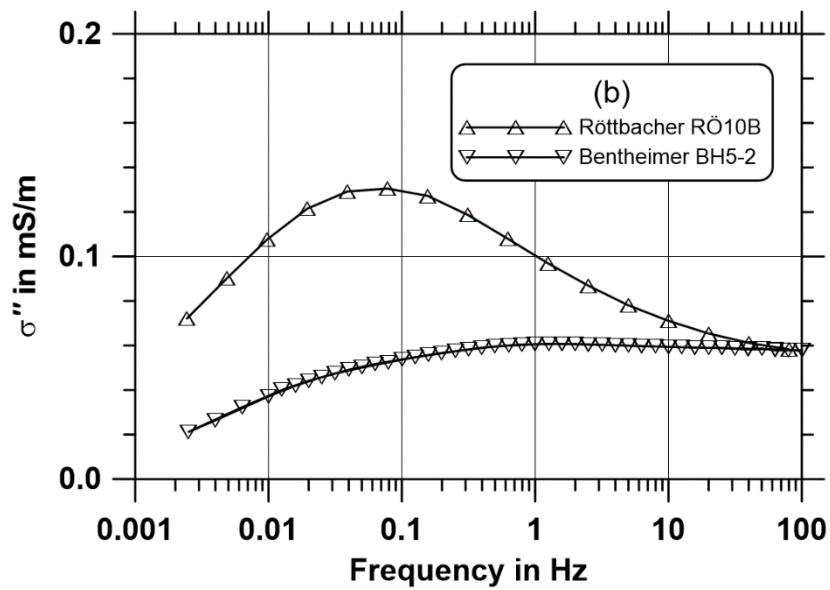


668
669

Figure 5: The NMR T_2 relaxation time distributions of samples BH5-2 and RÖ10B.

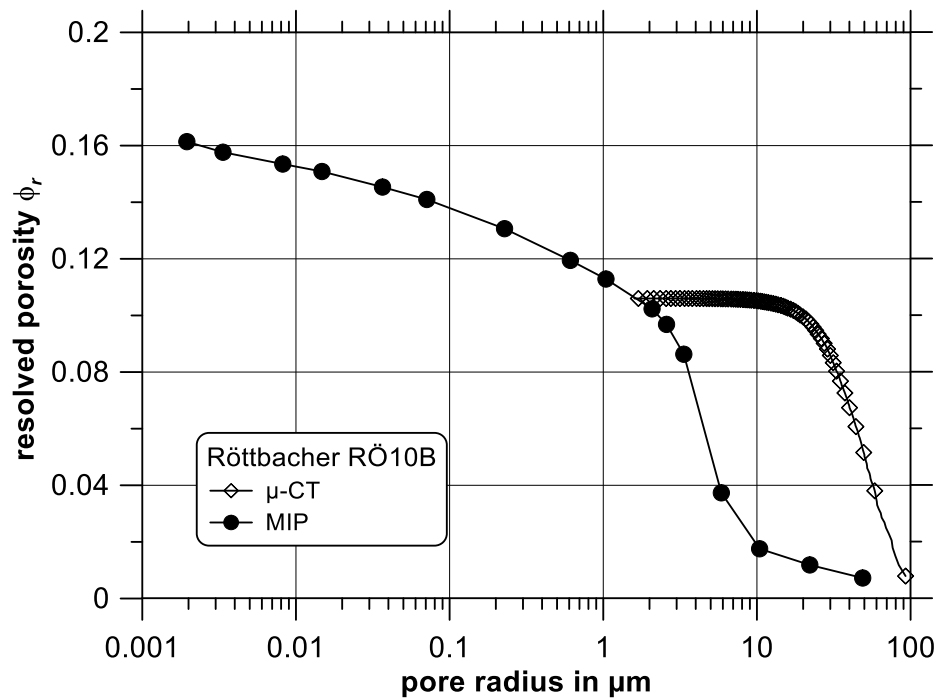


670



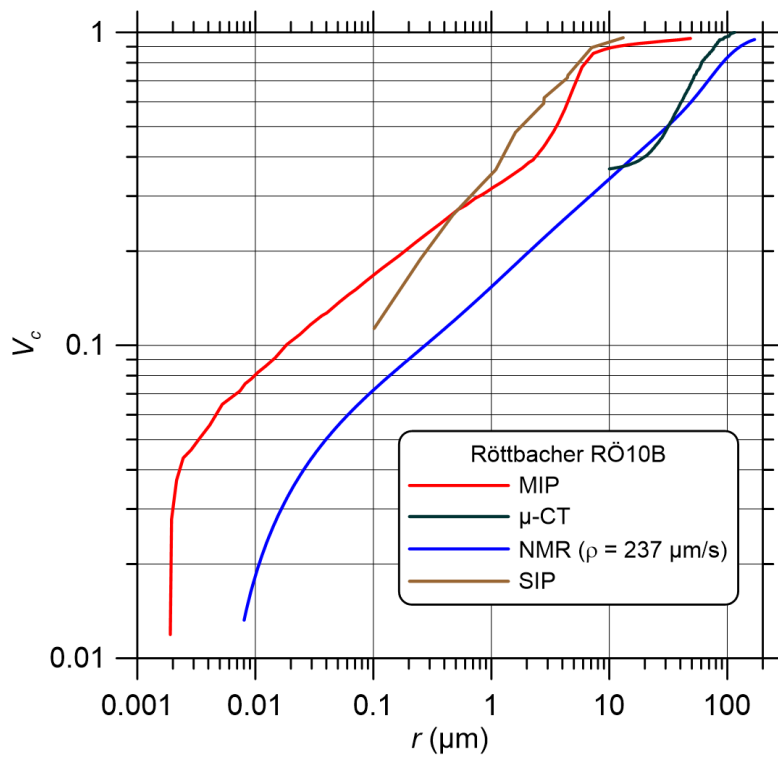
671
672
673
674
675
676

Figure 6: Measured complex conductivity spectra of samples BH5-2 and RÖ10B. a) real part of conductivity, b) imaginary part of conductivity.



677
678
679
680
681

Figure 7: The recognized porosity and pore size range of Röttbacher sandstone sample RÖ10B. The maximum porosity recognized by MIP is 0.166 and the maximum porosity recognized by μ -CT is 0.106.



682
 683
 684
 685
 686
 687
 688

Figure 8: The comparison of V_c - r curves determined from MIP, μ -CT, NMR and SIP for Röttbacher sandstone sample RÖ10B.